Bioinspiration & Biomimetics

PAPER

Investigation of chordwise functionally graded flexural rigidity in flapping wings using a two-dimensional pitch–plunge model

To cite this article: Joseph Reade and Mark Jankauski 2022 *Bioinspir. Biomim.* **17** 066007

IOP Publishing Bioinspir. Biomim. 17 (2022) 066007 https://doi.org/10.1088/1748-3190/ac8f05

Bioinspiration & Biomimetics

RECEIVED
15 April 2022

REVISED
2 August 2022

ACCEPTED FOR PUBLICATION
2 September 2022

PUBLISHED
3 October 2022

PAPER

Investigation of chordwise functionally graded flexural rigidity in flapping wings using a two-dimensional pitch–plunge model

Joseph Reade and Mark Jankauski*

Montana State University, Department of Mechanical & Industrial Engineering, Bozeman, MT, United States of America
* Author to whom any correspondence should be addressed.

E-mail: mark.jankauski@montana.edu

Keywords: flapping wings, unsteady vortex lattice method, reduced-order modeling, pitching-plunging airfoil, insect flight, structural dynamics

Abstract

Insect wings are heterogeneous structures, with flexural rigidity varying one to two orders of magnitude over the wing surface. This heterogeneity influences the deformation the flapping wing experiences during flight. However, it is not well understood how this flexural rigidity gradient affects wing performance. Here, we develop a simplified 2D model of a flapping wing as a pitching, plunging airfoil using the assumed mode method and unsteady vortex lattice method to model the structural and fluid dynamics, respectively. We conduct parameter studies to explore how variable flexural rigidity affects mean lift production, power consumption and the forces required to flap the wing. We find that there is an optimal flexural rigidity distribution that maximizes lift production; this distribution generally corresponds to a 3:1 ratio between the wing's flapping and natural frequencies, though the ratio is sensitive to flapping kinematics. For hovering flight, the optimized flexible wing produces 20% more lift and requires 15% less power compared to a rigid wing but needs 20% higher forces to flap. Even when flapping kinematics deviate from those observed during hover, the flexible wing outperforms the rigid wing in terms of aerodynamic force generation and power across a wide range of flexural rigidity gradients. Peak force requirements and power consumption are inversely proportional with respect to flexural rigidity gradient, which may present a trade-off between insect muscle size and energy storage requirements. The model developed in this work can be used to efficiently investigate other spatially variant morphological or material wing features moving forward.

1. Introduction

Flapping insect wings are highly compliant structures that deform under aerodynamic and inertial forces [1]. Deformation is believed to play a fundamental role in insect flight mechanics and has been shown to enhance aerodynamic force generation [2–4] and energetic efficiency [5–7]. Various structural features, including venation and corrugation, influence wing deformation under dynamic loading. These features also govern how the wing's mechanical properties vary in space. Experimental studies have shown that the flexural rigidity of the Hawkmoth *Manduca sexta* forewing, for example, varies one to two orders of magnitude over the wing's chord length [8]. This pronounced gradient may underpin wing responses that are aerodynamically and energetically favorable. However, it is not well understood how graded flexural rigidity influences flapping wing performance.

This is in part because models used to predict wing fluid–structure interaction (FSI) are computationally-intensive. They are consequently challenged by parameter studies that consider variable flexural rigidity or other morphological and material properties. Flapping wing FSI models usually rely on coupled finite element method (FEM) and computational fluid dynamic solvers (CFD) [9–13]. Flapping wings pose unique challenges to both of these numerical approaches. Given the finite, periodic rotation of the wing, stiffness matrices within FEM must be updated at each time interval of analysis, which increases computation times considerably [14]. CFD requires that the Navier–Stokes equations be solved across a discretized fluid domain [15], which could result in upwards of hundreds of thousands of equations to solve. Estimating wing deformation via coupled CFD/FEM may therefore span several hours per wingbeat in some cases.

Lower-order FSI models can decrease the computational requirements considerably. Simplifications in fluid and structural solvers, as well as converting the 3D problem to a 2D idealization, have yielded models that can be solved on the order of seconds. Some of the most common flapping wing FSI models treat the wing as a 2D pitching, plunging airfoil [2, 3, 7, 16, 17]. The airfoil represents a cross-section running along the chord of the insect's wing. Plunge represents the primary flap rotation and pitch represents the rotation the wing experiences about its leading edge. The 2D pitch–plunge framework neglects some of the physics that play a role in true 3D flapping, such as spanwise bending [18], spanwise flow [19] and wingtip effects [20]. Despite lower quantitative accuracy relative to 3D models, 2D models can quickly identify solution trends and thus can establish foundational knowledge that may be subsequently extended to more computationally intensive 3D modeling. For this purpose, they have been widely utilized to investigate several aspects of flapping wing mechanics. For example, Yin and Luo used a pitch–plunge model to show that, when a wing's deformation was dominated by external flows rather than inertia, it had better power efficiency [7]. Tian *et al* used this framework to understand how asymmetry between the wing's deformation during upstroke and downstroke affected forward flight [17]. Vanella *et al* demonstrated that a super-harmonic resonance may favorably influence the wing's lift to drag ratio at low Reynold's numbers [2]. Mountcastle and Daniel investigated how variable wing kinematics and structural properties affected the wing's lift generation [3].

Despite the contributions of these works and others, the influence graded flexural rigidity has on flapping wing aeromechanics remains understudied. The objectives of the present research are to (1) develop a reduced-order FSI model of a flapping, flexible insect wing treated as a pitching plunging airfoil, and (2) to use this model to understand how chordwise graded flexural rigidity affects wing dynamics. Specifically, we evaluate lift, power and the forces required to drive the wing. We employ a number of assumptions to simplify the wing structure and flapping kinematics in this study. First, because we treat the wing as a 2D pitching, plunging airfoil, spanwise flow, spanwise bending and wingtip losses associated with 3D motion are neglected. Second, we neglect complex venation patterns, cross-sectional curvature and spatially-variable material properties that may affect the wing's local flexural rigidity. We instead assume that spatial variation of flexural rigidity is driven by chordwise variations of wing thickness, since vein thickness reduces dramatically along the chord in many insect wings [21]. Because of these assumptions, the model developed in this work is not suitable for high-fidelity fluid or structural calculations of real insect wings. It is instead intended to isolate and study variable flexural rigidity in a simpler setting.

The remainder of this manuscript is organized as follows. First, we derive the FSI framework using the assumed mode method (AMM) to model the structure and unsteady vortex lattice method (UVLM) to model the fluid. Next, we apply the model to numerically simulate the response of a wing with similar properties to a Hawkmoth *Manduxa sexta* (*M. sexta*) forewing. We explore the aerodynamics and energetic requirements of the wing under hovering flapping circumstances, and conduct a parameter study to determine how these quantities are influenced by variable kinematics. We conclude by discussing the broader implications of this research on the study of insect flight and insect-inspired robotics.

2. Theory

2.1. Structural model

In this section, we derive the equation of motion governing the wing's deformation via the Lagrangian approach. We treat the wing as an Euler–Bernoulli beam, where the leading edge is clamped and the trailing edge is free to deflect. Wing deformation is calculated using the AMM, where the total deflection is a linear combination of the wing's eigenfunctions. This work expands upon the structural model derived in [22].

First, we first define two reference frames; an inertial $X-Y-Z$ frame that is fixed in space, and a body-fixed $x-y-z$ frame that translates and rotates with the wing's rigid body motion (figure 1). Note that the gravity would act in the $+Y$ direction, and thus the wing must produce lift in the $-Y$ direction in order for the insect to remain aloft. The origin O of the $x-y-z$ frame is located at the leading edge of the wing. O is subject to prescribed plunging $Z(t)$ and the wing experiences prescribed pitching $\theta(t)$ about O. The $x-y-z$ frame has angular velocity

$$\boldsymbol{\Omega} = \dot{\theta}\boldsymbol{e}_x \tag{1}$$

The position $\boldsymbol{R}$ of a differential mass element $\mathrm{d}m$ relative to the body-fixed frame is the sum of three component vectors (e.g., $\boldsymbol{R} = \boldsymbol{r}_1 + \boldsymbol{r}_2 + \boldsymbol{r}_3$), where

$$\boldsymbol{r}_1 = Z(t)\boldsymbol{e}_Z = Z(t)\sin\theta\boldsymbol{e}_y + Z(t)\cos\theta\boldsymbol{e}_z \tag{2}$$

$$\boldsymbol{r}_2 = y\boldsymbol{e}_y \tag{3}$$

$$\boldsymbol{r}_3 = w(y,t)\boldsymbol{e}_z \tag{4}$$

Above, $\boldsymbol{r}_1$ describes the displacement associated with the plunging motion, $\boldsymbol{r}_2$ describes the position of $\mathrm{d}m$ at a location y along the wing's chord, and $\boldsymbol{r}_3$ describes

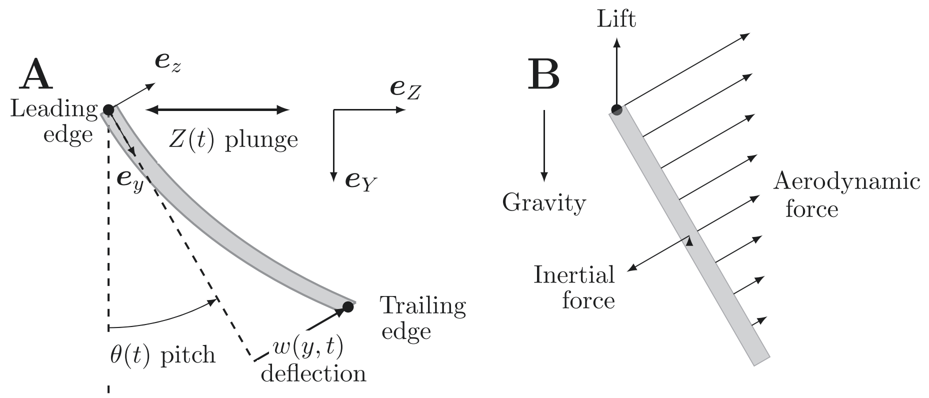

Figure 1. (A) Reference frames and pitch–plunge motion, (B) free-body diagram of forces acting on the wing and gravity vector to show orientation. Cartesian grad applies to both panels. The black circle in both panels indicates where the wing would meet insect body.

an infinitesimal out-of-plane wing deflection w. In-plane deflection is neglected. The velocity of dm is

$$\dot{\boldsymbol{R}} = [\dot{Z}\sin\theta - w\dot{\theta}]\,\boldsymbol{e}_y + [\dot{Z}\cos\theta + y\dot{\theta} + \dot{w}]\,\boldsymbol{e}_z \tag{5}$$

and the acceleration of dm is

$$\ddot{\boldsymbol{R}} = [\ddot{Z}\sin\theta - 2\dot{w}\dot{\theta} - w\ddot{\theta} - y\dot{\theta}^2]\boldsymbol{e}_y \ \ldots$$
$$+ [\ddot{Z}\cos\theta + \ddot{w} + y\ddot{\theta} - w\dot{\theta}^2]\boldsymbol{e}_z \tag{6}$$

While $\ddot{\boldsymbol{R}}$ is not required to derive the equation of motion, it is necessary to calculate power consumption and inertial forces and moments as detailed later. We expand wing deflection $w(y,t)$ in terms of mass-normalized mode shapes ϕ_k and modal responses q_k as

$$w(y,t) = \sum_{k=1}^{\infty} \phi_k(y)\, q_k(t). \tag{7}$$

In practice, only a finite number of modes are used. In this implementation, we include only the first mode (see section 3). The wing's total kinetic and potential energies are subsequently formulated. Applying Lagrange's equation, we arrive at the equation of motion governing modal response q_k as

$$\ddot{q}_k + 2\zeta_k\omega_k\dot{q}_k + (\omega_k^2 - \dot{\theta}^2)q_k = -\lambda_k\ddot{Z}\cos\theta - \psi_k\ddot{\theta} + Q_k \tag{8}$$

where ω_k and ζ_k are the wing's kth natural frequency and damping ratio, respectively. Note that the viscous damping term is not derived explicitly through the energy formulation and is instead included as an empirical correction term. Constants λ_k and ψ_k are obtained by integrating the mode shape over the wing's mass domain, or

$$\lambda_k = \int_m \phi_k \,\mathrm{d}m \tag{9}$$

$$\psi_k = \int_m y\phi_k \,\mathrm{d}m \tag{10}$$

Equation (8) shows that the wing's stiffness is time-varying and dependent on the wing's pitching rate and stationary natural frequency. The first excitation term to the right-hand side of equation (8) is a plunge-dominated inertial term proportional to the linear acceleration of the wing. The second excitation term is a pitch-dominated inertial term modulated by the wing's angular acceleration. The non-conservative generalized load Q_k is obtained by integrating the projection of an aerodynamic force distribution onto the mode shape

$$Q_k = \int_c \phi_k(\mathrm{d}\boldsymbol{F}_{\mathrm{aero}}\cdot\boldsymbol{e}_z)\,\mathrm{d}y \tag{11}$$

where d$\boldsymbol{F}_{\mathbf{aero}}$ is the aerodynamic force per unit length, discussed the following section.

2.2. Fluid model

We use a modified UVLM approach to predict the flow and estimate the force distribution over the wing. Our method is based on that described in [23]. Only a high-level description of the model is given here. For additional detail on the mathematical derivation, please refer to appendix A.

UVLM is based on potential flow theory. The flow is assumed to be irrotational, except on the surface of the wing and in the wake that is shed from the trailing edge, and is incompressible throughout. By modeling the wake, we account for unsteady effects such as added mass. Viscous effects are not accounted for. Using the maximum plunge rate and chord width as the characteristic speed and length respectively, the Reynolds number of the wing simulated in this work under normal hovering conditions is about 5000 (see section 3). This indicates that inertial aerodynamic forces will far exceed viscous aerodynamic forces, and hence we believe the inviscid assumption is reasonable in this study.

The wing is discretized into N_p panels, each of length ds (figure 2). On each panel, a bound vortex and control point are located 0.25 ds and 0.75 ds from the leading edge of the panel, respectively. Additionally, a wake vortex is shed from the trailing edge of the

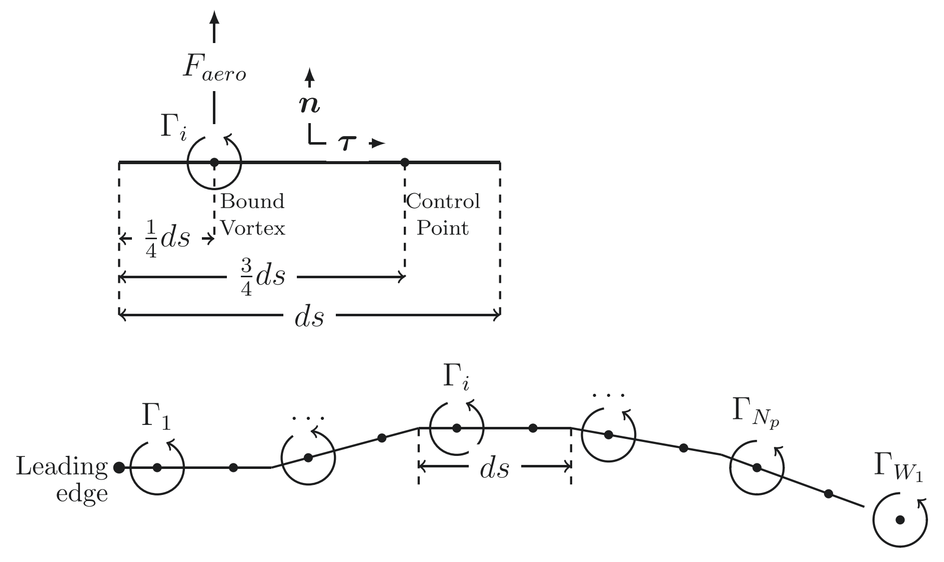

Figure 2. Wing discretization used by UVLM.

wing at each time step, with the wake being truncated at N_{w} vortices. A bound vortex induces a flow velocity around itself that diminishes with distance. The flow velocity at any point in space that is induced by a vortex is given by the Biot–Savart law. Then, according to the Kelvin–Helmholtz theorem for an ideal fluid, the total circulation around a closed contour must remain constant. Since the initial state of the fluid flow is at rest with zero vorticity throughout, this implies that the total vorticity, found by summing the strengths of the bound and wake vortices, is zero at each time step. This condition is used to calculate the strength of the wake vortices.

Flow may not travel through the solid surface of the wing, meaning that the component of velocity normal to the surface is zero. Because there are a finite number of bound vortices, the non-penetration condition cannot be satisfied across an entire panel, so the control point is chosen as the location where it must hold true. By simultaneously enforcing the non-penetration condition at all control points on the wing, as well as the Kelvin–Helmholtz condition, the strengths of the bound vortices can be determined. Advected wake vortices are placed a fixed distance aft of the trailing edge. All existing wake vortices are advected with the local flow. Finally, the aerodynamic force on the wing is determined using the unsteady Bernoulli equation.

2.3. Force, moments and power

Flight is the most energetically expensive mode of locomotion per unit of time, and thus it is essential to understand how the wing's structural dynamics underpin low energetic expenditures. In this section, we derive expressions based on modal responses to calculate flapping wing moments, forces and instantaneous power.

Total power consumption is broken into two components: inertial power and aerodynamic power. Inertial power is required to move the wing mass through space—if the wing was operated in a vacuum, inertial power would equal to total power. Inertial power of a rotating, translating system is

$$P_{\text{inertial}} = \boldsymbol{F}_O \cdot \dot{\boldsymbol{r}}_1 + \boldsymbol{M}_O \cdot \boldsymbol{\Omega} \tag{12}$$

where $\boldsymbol{F}_O$ is the inertial force at O and $\boldsymbol{M}_O$ is the inertial moment about the leading edge. The inertial force is the wing's spatiotemporal acceleration integrated over the wing's mass, is

$$\begin{aligned}\boldsymbol{F}_O = &\left[m\ddot{Z}\,\sin\,\theta - \dot{\theta}^2\xi - \sum_{k=1}^{\infty}(2\dot{q}_k\dot{\theta}\lambda_k + q_k\ddot{\theta}\lambda_k)\right]\boldsymbol{e}_y \\ &+ \left[m\ddot{Z}\,\cos\,\theta + \ddot{\theta}\xi \;- \sum_{k=1}^{\infty}(q_k\dot{\theta}^2\lambda_k - \ddot{q}_k\lambda_k)\right]\boldsymbol{e}_z\end{aligned} \tag{13}$$

where m is the mass of the wing and ξ is a constant defined by

$$\xi = \int_m y\,\mathrm{d}m. \tag{14}$$

The inertial moment about O is

$$\begin{aligned}\boldsymbol{M}_O = &\left[\ddot{Z}\xi\,\cos\,\theta + I_{xx}\ddot{\theta} + \sum_{k=1}^{\infty}\left(\ddot{q}_k\phi_k - \ddot{Z}q_k\lambda_k\,\sin\,\theta\right.\right. \\ &\left.\left.+\,\ddot{\theta}q_k^2 + 2q_k\dot{q}_k\dot{\theta}\right)\right]\boldsymbol{e}_x\end{aligned} \tag{15}$$

where I_{xx} is the wing's mass-moment of inertia about O. The aerodynamic power is the power required to overcome the fluid forces acting against the wing, given by

$$P_{\text{aero}} = \int_{\text{chord}} \mathrm{d}\boldsymbol{F}_{\text{aero}} \cdot \dot{\boldsymbol{R}}\,\mathrm{d}y \tag{16}$$

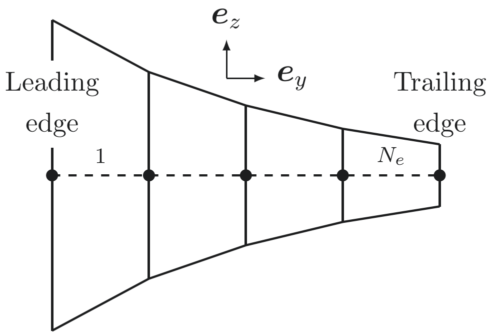

Figure 3. Wing discretization with exponential thickness distribution. Nodes $2, \ldots, N_e + 1$ may experience vertical displacement and rotation, while the leading-edge node is clamped. Wing thickness is exaggerated.

where $\mathrm{d}\boldsymbol{F}_{\text{aero}}$ is the aerodynamic force at some point on the wing as computed by the UVLM.

3. Numerical simulation

Here, we describe the numerical parameters used to simulate the dynamic response of the wing. We use the FEM to convert the wing from a continuous domain to a discrete domain (see appendix B). The finite element discretization is implemented using a custom in-house MATLAB (Ver. 2020b) code. The wing is discretized into N_e beam elements each with two degrees-of-freedom (vertical displacement and rotation) at each node. We use spatially variable wing thickness to modulate local flexural rigidity, since wing flexural rigidity is affected by thickness and Young's modulus and the latter is kept constant (figure 3). The wing thickness decays exponentially from leading edge to trailing edge, with the thickness t at chordwise location y described by

$$t(y) = t_{\text{LE}} e^{-a\frac{y}{c}}, \tag{17}$$

where t_{LE} is the leading edge thickness, c is the chord length and a is the decay rate. Values of a range from 0 to 1.6, which correspond to leading-to-trailing-edge taper ratios $t_{\text{TE}}/t_{\text{LE}}$ from 1.0 (uniform thickness) to 0.2 (highly tapered). The most tapered case results in a two orders-of-magnitude decrease in flexural stiffness over the chord, which encompasses the range of chordwise-stiffness distributions reported in *Manduca sexta* [8]. Wing mass is maintained at 45 mg across all taper ratios tested. Consequently, each wing has an average thickness of 45 μm, but the leading edge thickness t_{TE} varies with taper ratio. The maximum leading edge thickness considered is 90 μm for the most tapered wing. We also simulate rigid wings across all taper ratios to compare their performance against flexible wings.

We use 40 panels, 40 finite elements, 100 wakes and 200 time steps per wingbeat for all numerical studies. The convergence studies that informed these parameters are detailed in appendix C. We neglect any modes associated with frequencies at least ten times higher than the flapping frequency, as the contribution of these modes is expected to be small. The second natural frequency was 360 Hz for a homogeneous wing, which is roughly 14 times greater than the flapping frequency of 25 Hz. All other stiffness distributions tested have a greater second natural frequency. Therefore, only the first mode was retained for simulations. We use the MATLAB (Ver. 2020b) explicit ode45 solver to simulate the response of the wing. For all simulations, we calculate wing deflection, forces at the leading edge and total power required to flap the wing. We also calculate mean lift-to-power as proxy for flight efficiency.

Table 1. Wing parameters.

Symbol	Description	Value	Units
E	Young's modulus	10	GPa
c	Chord length	2	cm
b	Span	5	cm
m	Mass	45	mg
t_{avg}	Average thickness	45	μm
ρ	Density	1000	kg m^{-3}
ζ_1	First modal damping ratio	0.05	—
Z_0	Plunge amplitude	2.62	cm
θ_0	Pitch amplitude	45	$^\circ$
β_z	Pitch–plunge phase difference	-90	$^\circ$
ω	Flapping frequency	25	Hz

Wing morphology and flapping kinematics are based approximately on the *M. Sexta* [8, 24, 25] and are summarized in table 1. Flapping kinematics assume hovering flight. Pitch and plunge are idealized as purely harmonic with a frequency of 25 Hz and a phase difference of -90°. The plunge amplitude was approximated by the distance traveled by the semispan (x = span/2) of a three-dimensional wing experiencing a flap amplitude of 60°. The Young's modulus and density were estimated from measurements on insect cuticle [26, 27].

Prior to numerical simulations on tapered wings, we performed a validation study on homogeneous flexible wings to benchmark the accuracy of our model (see appendix D). Lift coefficients generated via our reduced-order model were compared to those generated by a higher-fidelity model [7]. Note that the flapping kinematics used in the validation study vary modestly from those used in the hovering case described in this paper. The lift coefficients predicted for each model had similar magnitude, but were modestly out of phase.

4. Results

In this section, we show how taper ratio influences flexural rigidity and thus the dynamics of flapping wings. First, we determine how taper affects the wing's first natural frequency and mode shape. Next, we calculate wingtip deflection, lift, power consumption and total forces acting at the wing's leading edge

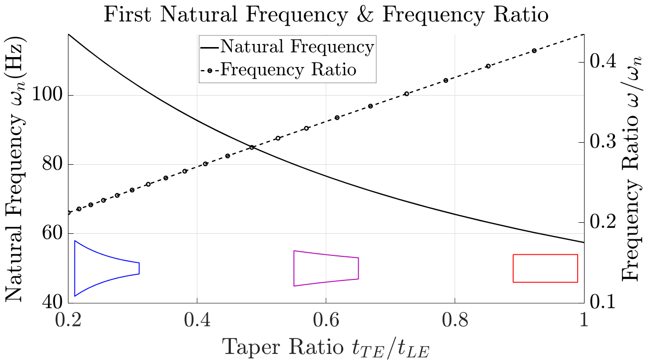

Figure 4. First natural frequency (solid line) and frequency ratio (dashed line) as a function of chordwise wing taper. Approximate airfoils indicating the taper are shown at the bottom of the figure, with taper ratios of 0.2, 0.6, and 1 from left to right. Flapping frequency is assumed to be 25 Hz.

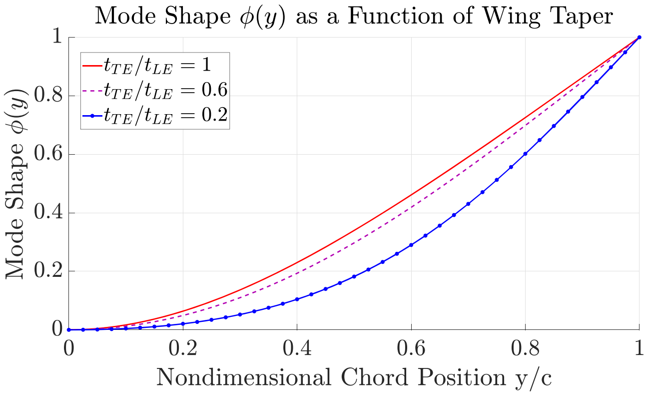

Figure 5. The bending mode used to calculate wing deflection. Mode shapes presented in this plot are normalized by the maximum value at the trailing edge.

for a wing flapping with hovering kinematics. We then conduct a parameter study to examine how deviations from hovering kinematics affect wing performance.

4.1. Natural frequencies & mode shapes

The wing's natural frequency affects deflection magnitude and consequently, the aerodynamic forces that arise from flapping. Certain flapping-to-natural frequency ratios have been shown to improve the aerodynamic and energetic performance of flapping wings [2, 5, 6]. Here, we explore how variable flexural rigidity influences the wing's natural frequency to provide context to the dynamic studies described in the following sections.

Over the range of taper ratios considered, the wing's natural frequency varies from about 57 to 115 Hz (figure 4). Assuming a flap frequency of 25 Hz, this coincides to a flapping-to-natural frequency ratio range from 0.21 to 0.44. Natural frequencies corresponding to the first torsional mode in *M. sexta* forewings have been reported between 75–95 Hz [25, 28], which are represented by taper ratios from about 0.4 to 0.5. Note that the first mode in the *M. sexta* forewing corresponds to a bending mode, however since our 2D model does not account for spanwise deformation, it is more appropriate to compare our computed natural frequencies to torsional modes where deformation varies predominately over the wing chord. Though the bending mode in *M. sexta* wings has a lower natural frequency (≈60–70 Hz, [25, 28]) than the twisting mode, this does not necessarily imply the bending mode is more important. The insect flaps at about 25 Hz, and previous studies have shown flapping excites frequencies at odd multiples of the wingbeat frequency. Consequently, twisting may be as significant as bending to wing deformation.

As the taper ratio decreases from 1 to 0.2, the wing's local area moment of inertia and mass increase near the leading edge and decrease towards the trailing edge. As a result, the wing's natural frequency is inversely proportional to taper ratio (figure 4). The most tapered wing has a natural frequency nearly double that of the homogeneous wing. Mode shapes associated with tapered wings tend to bend more around the center of the chord, while bending is localized towards the leading edge in homogeneous wings (figure 5). This is consistent with torsional mode shapes measured in *M. sexta* forewings [25].

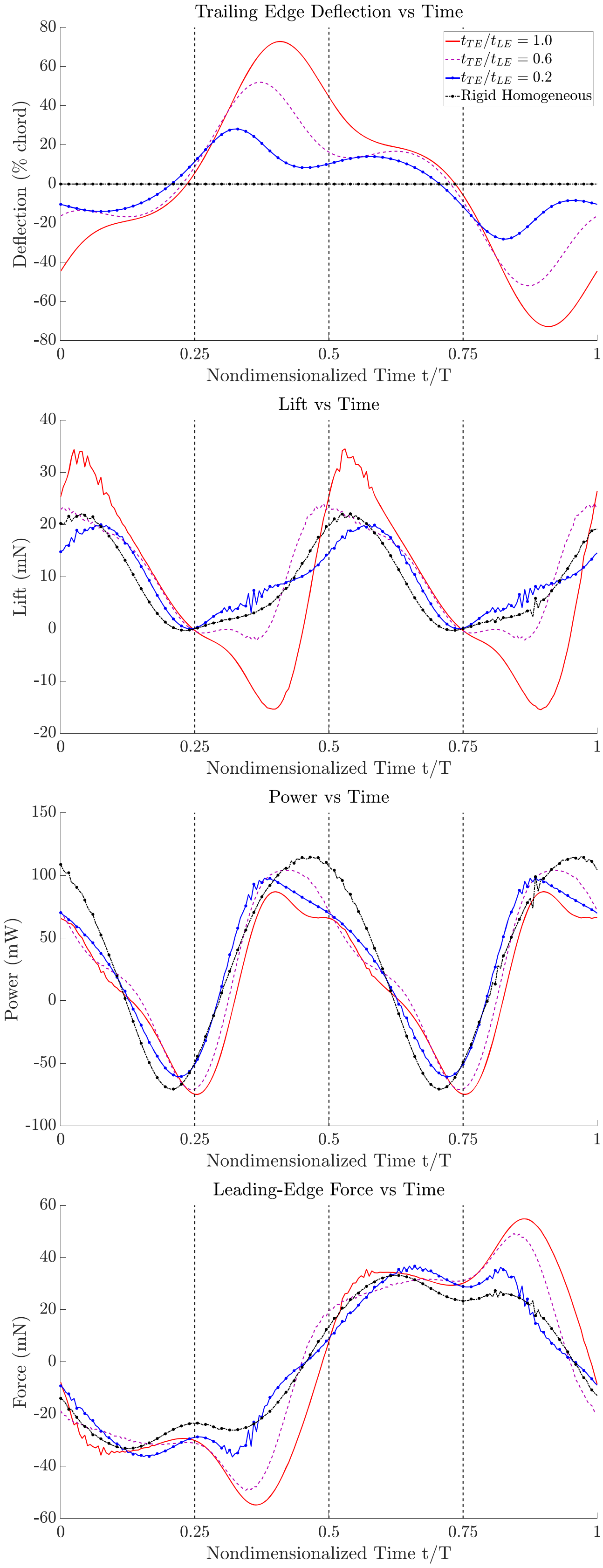

Figure 6. Comparison of lift, power, leading edge force, and wing tip deflection for several taper ratios using kinematics in table 1.

4.2. Flapping with hovering kinematics

We now examine the wing's dynamic response assuming the flapping kinematics described in table 1. Wing deflection, lift, power and leading edge force are shown for various taper ratios in figure 6. Quantities are reported as a function of wingbeat fraction t/T, where t is time and T is the wingbeat period. All quantities are taken once the wing has achieved steady-state. We use mean power as a proxy for energy consumption. This assumes negative power is elastically stored in the insect exoskeleton and that this stored potential energy can be recycled to offset positive power requirements. Then, we use the Z component of total leading edge force $\mathbf{F}_{\mathrm{T},XYZ}$ to approximate the forces the insect flight muscle must produce in order to flap the wing. $\mathbf{F}_{\mathrm{T},XYZ}$ is defined with respect to the inertial coordinate system and is inclusive of both aerodynamic and inertial forces. The Z component of $\mathbf{F}_{\mathrm{T},XYZ}$ (simply leading edge force hereafter) is a better proxy for muscle forces than total moment $\mathbf{M}_{\mathrm{T}}$, since the literature suggests wing pitching arises passively from inertial and aerodynamic forces [29].

Calculated deflections appear to be consistent with reported values for *M. sexta* [24]. Previous studies reported the angle of rotation between the leading edge and the trailing edge, which is an aggregate quantity influenced both by the rigid body pitch angle and trailing edge deflection. Angles of rotation were typically around 45° for chords proximal to the insect body and 65° for chords distal to the insect body. Our model predicted angles of rotation of approximately 59° when for a taper ratio of 0.2 and 71° for a taper ratio of 1. While the homogeneous wing resulted in an angle of rotation greater than reported values, the tapered wings matched fairly well. Aerodynamic forces are also consistent with those produced by *M. sexta*. Assuming the insect has a body mass of 2.0 grams [30], a wing pair produces sufficient lift to hover when taper ratios are between about 0.27 and 0.65. This corresponds to a natural frequency range of about 70 to 109 Hz.

As chordwise wing taper ratio increases, both wingtip deflection amplitude and primary response phase (taken with respect to plunge) decrease (figure 6). The lower deflection is due to the tapered wing being stiffer than the homogeneous wing, evidenced by the higher natural frequency (figure 4). Peak deflection moves away from the mid-stroke ($t/T = 0, 0.5$) and towards the stroke reversals ($t/T = 0.25, 0.75$) as wing flexibility increases. This indicates that deflection in highly tapered wings is more influenced by the plunging inertial force and less by the aerodynamics, as plunging acceleration $\ddot{Z}$ is at a maximum while the aerodynamic force is minimized at stroke reversal.

Table 2. Peak deflection, mean lift, mean power and peak leading edge force for various taper ratios assuming normal flapping kinematics. Rigid wing is assumed to have uniform thickness.

Taper ratio	1.0	0.6	0.2	Rigid
Peak deflection (mm)	14.6	10.4	5.6	0
Mean lift (mN)	7.19	10.1	9.47	8.89
Power (mW)	15.5	26.4	28.8	33.6
Peak leading edge force (mN)	54.8	49.2	36.7	33.2

Chordwise wing taper has a large effect on lift production. While the homogeneous wing generated the highest peak lift, its time-averaged lift was 20 to 30 percent lower than that of the other wings (table 2). This can be partially attributed to the large troughs in lift occurring at $t/T \approx 0.375, 0.875$, when the plunging motion of the wing reverses. These troughs are not seen with the stiffer wings. The lowest point in the trough roughly corresponds to the peak deflection experienced by the wing. Separating lift into steady and unsteady components, we see that the negative lift is largely driven by the steady component. When the wing undergoes large deflections, it reduces the effective angle of attack and creates an adverse camber that biases lift in the positive Y direction. As the taper becomes more pronounced and wing stiffness increases, the lift contribution from the steady component increases while that of the unsteady component is reduced.

Mean power is sensitive to taper ratio as well. The primary effect of wing deformation is seen at the mid-stroke ($t/T = 0, 0.5$), where peak power is lower for the flexible wings compared to the rigid wing. At that instant, the flexible wings are bent backwards due to aerodynamic forces, and their angle of attack is lower compared to that of the rigid wing. As a result, mean power is lower for the flexible wing compared to the rigid wing (table 2). While mean power reduces with taper ratio, peak leading edge forces increase. The most flexible wings experience the largest leading edge forces, where the peaks in forces coincide approximately with peak deflections. This indicates that the inertial and aerodynamic forces associated with elastic deformation increase the leading edge forces required to sustain the prescribed kinematics of O.

4.3. Deviations from hovering kinematics

In this section, we explore the sensitivity of the wing response to kinematic deviations from the hovering flapping kinematics shown in table 1. We characterize the influence of taper ratio on lift, power, leading edge force and mean lift-to-power for various sets of flapping kinematics.

4.3.1. Pitch amplitude

First, we investigate how pitch amplitude affects wing dynamics. Rigid-body pitch angle is difficult to characterize in flexible insect wings. We define rigid body pitch as the angle between the leading edge and trailing edge assuming the wing is rigid (figure 1). However, if the trailing edge deforms out-of-plane, the perceived pitch angle between the leading edge

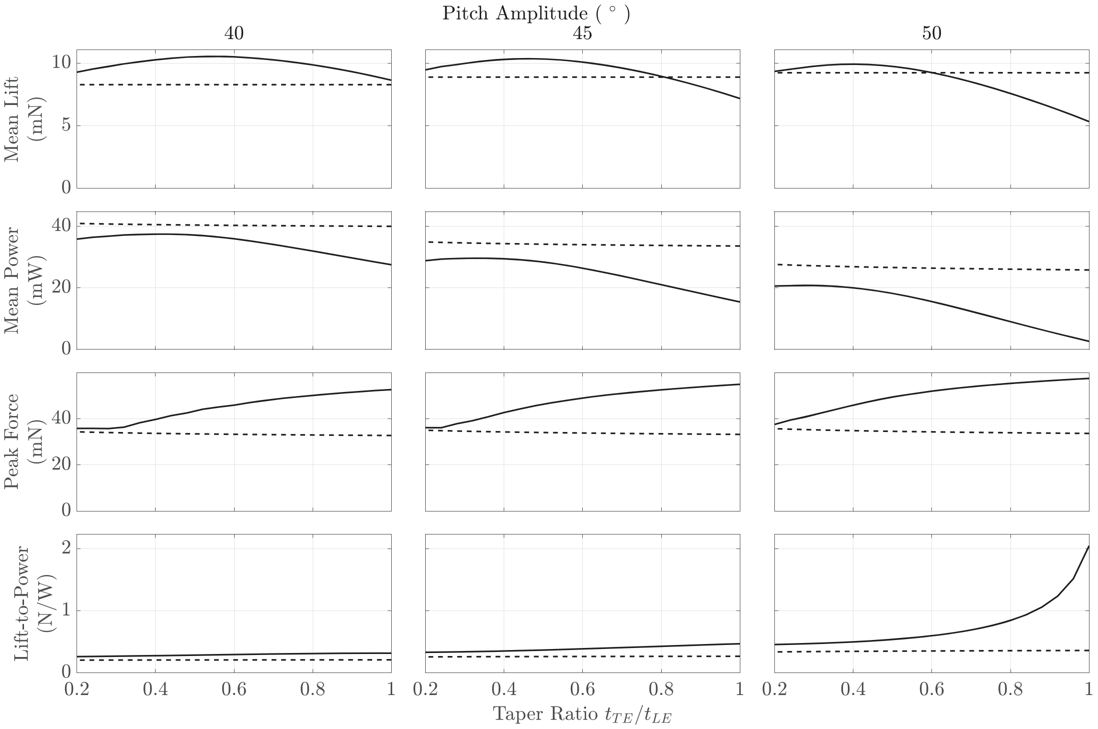

Figure 7. Study of pitch amplitude. The flexible and rigid wing values are represented by the solid and dashed lines, respectively.

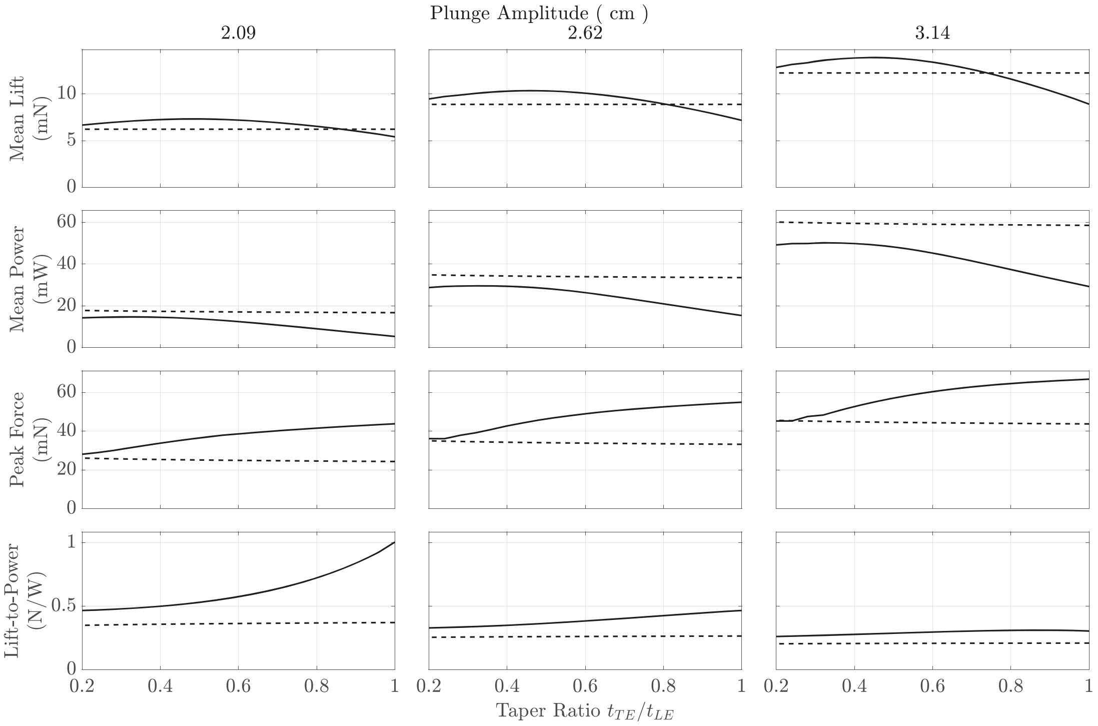

Figure 8. Study of plunge amplitude. The flexible and rigid wing values are represented by the solid and dashed lines, respectively.

and trailing edge will increase. All insect wings experience some deformation at the trailing edge in practice, and thus pitch amplitudes reported in the literature may overestimate rigid body pitch. We tested several values of rigid-body pitch amplitude to examine how wing performance is affected by variations in this quantity (figure 7).

Lift and power consumption are both strongly impacted by pitch amplitude. Pitch amplitude significantly affects mean lift in highly flexible wings, but only modestly affects lift in stiffer wings. When highly tapered, the wing produced nearly constant lift regardless of the pitching amplitude. By contrast, the highly flexible homogeneous wing is more sensitive to pitch amplitude. The wing experiences similar deformation under both pitch angles, but the effective angle of attack is decreased by the higher pitch angle in addition to the deflection-induced camber and the downwash caused by the wake vortices. Around stroke reversal in the 50° pitching case, the aerodynamic force is heavily weighted towards the leading edge, reducing both lift and power consumption. A byproduct of this is that the taper ratio associated with maximum lift decreases with increasing pitch amplitude. These results also demonstrate that there is an optimal taper ratio which maximizes lift generation, and that this optimal taper ratio depends on pitch amplitude.

Power consumption of the flexible wing is lower than that of the rigid wing in all cases. The mean power versus taper ratio curve is concave, with the location of the maxima contingent on pitch amplitude. The low energy requirement of the flexible wing at high pitch amplitude is due to the wing bending out of the way and minimizing aerodynamic loads, though this adversely affects lift generation. Mean lift-to-power increases with taper ratio, but is relatively stationary in the range of taper ratios that produce sufficient lift to hover. Across the taper ratios considered, the mean lift-to-power of the flexible wing is higher than that of the rigid wing.

Peak leading edge force is largely unaffected by the pitching angle. Forces in general are dominated by the plunging inertial and aerodynamic forces rather than the pitching inertial force. The pitching motion accounts for only 19% of the peak leading edge force in a homogeneous flexible wing and 14% in a wing with a taper ratio of 0.2. On the other hand, peak leading edge force is sensitive to taper ratio. The lowest leading edge forces occur in the most tapered wing, presumably because the wing's center of mass is closer to the point of rotation. This reduces the inertial forces associated with pitching. The largest leading edge forces occur in the untapered wing, since the center of mass is further from the point of rotation and the wing experiences larger deflections.

4.3.2. Plunge amplitude

Some insects have been shown to increase their flapping amplitude to increase lift generation [31]. Within the pitch–plunge model, this is akin to increasing the plunge amplitude. We tested three different values of plunge amplitude to identify how variation of this parameter affected lift, mean power and peak leading edge forces (figure 8).

Plunge amplitude impacts each quantity strongly. Raising the plunge amplitude increases the distance and velocity of the wing during each stroke. As expected, this increases the lift, power, and leading edge force. Mean lift in flexible wings does not increase proportionally to the plunge velocity squared as might be expected from conventional steady aerodynamic theory. A possible reason for this is that the increased velocity generates higher aerodynamic forces on the wing, which in turn leads to higher deflections and reduced angle of attack, meaning that increasing the plunge amplitude and velocity results in diminishing returns. Mean lift in stiffer wings more closely scales with plunge velocity squared.

For a stationary airfoil subject to a uniform free-stream velocity, aerodynamic power scales with the free-stream velocity cubed [32]. We observe that the mean power scales nearly cubically with plunge velocity in rigid wings. In the highly tapered wing, the mean power requirement is nearly identical to that of a rigid wing at low plunge amplitudes. However, at higher plunge amplitudes, the disparity between power requirements is larger. The increased deflection arising from plunge amplitude likely decreases the effective drag on the wing, thereby reducing the power required by the flexible wing. This also explains why power decreases with taper ratio for all plunge amplitudes considered, though mean lift decreases above a certain taper ratio as well. The optimal taper ratio thus falls somewhere between providing sufficient lift to fly while requiring low energetic expenditures. Since the lift-to-power ratio increases monotonically with taper ratio for all plunge amplitudes considered, the optimal configuration corresponds to the highest taper ratio that satisfies the roughly 10 mN mean lift constraint.

Increasing the plunge amplitude increases the peak leading edge force for all wings considered, since the increased plunging amplitudes lead to larger linear accelerations and aerodynamic forces. As plunge amplitude increases, the contribution of the plunging force actually decreases slightly for all tested taper ratios. This is because the aerodynamic forces acting on the wing are more sensitive to increases in plunging amplitude than the plunging inertial forces are.

4.3.3. Pitch–plunge phase

Hawkmoths have been shown to adjust the relative phase of activation between their two flight muscle groups in response to visual stimuli [33], which influences the relative phase between their wing's flap and pitch rotations. It is plausible that modulation of the phase between kinematic parameters is responsible for some maneuvers during flight. Here, we explore how the relative phase between wing pitching and plunging motions affects flapping wing aeromechanics. Mean lift, power and peak leading edge forces are shown as a function of taper ratio for various pitch–plunge phase differences in figure 9.

Mean lift is fairly influenced by deviations in pitch–plunge phase. Increasing the phase to −75° increases the highest achievable lift in both flexible

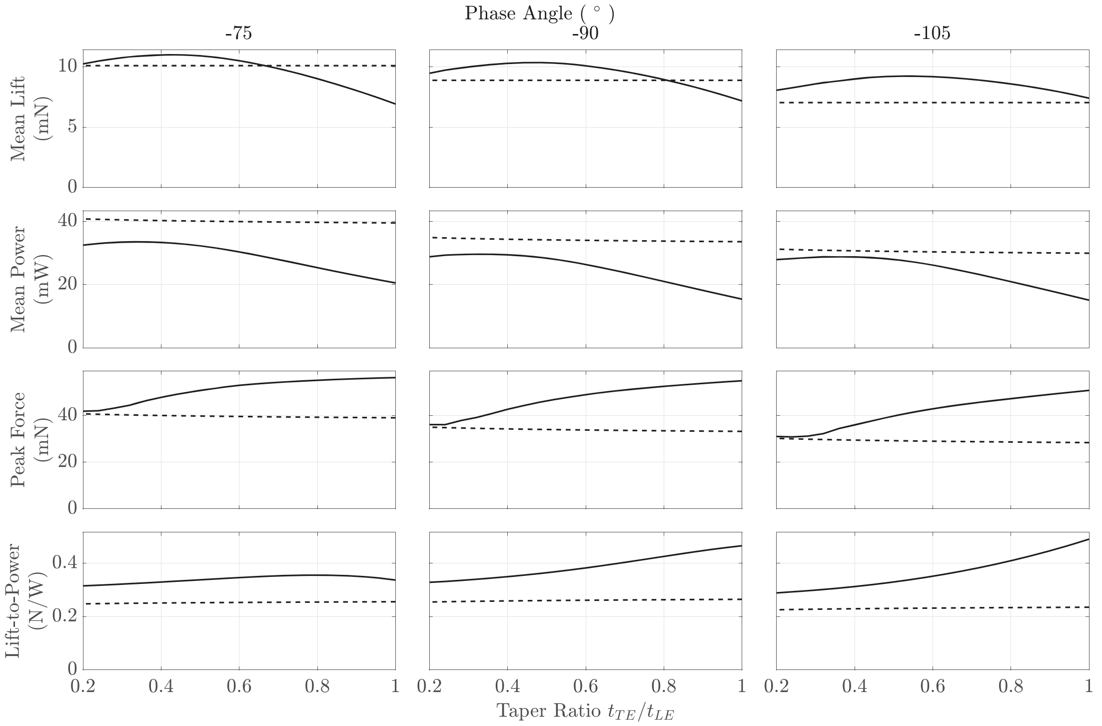

Figure 9. Study of pitch–plunge phase offset. The flexible and rigid wing values are represented by the solid and dashed lines, respectively.

and rigid wings, whereas decreasing the phase to −105° decreases highest achievable lift. Flexible wings across all taper ratios produce higher lift than rigid wings for a pitch–plunge phase of −105°, but for a pitch–plunge phase of −75°, flexible wings only produce mean lift than rigid wings for low taper ratios. Similar to trends observed in pitch amplitude, the taper ratio associated with greatest mean lift varies modestly with respect to pitch–plunge phase.

Mean power in general decreases when pitch–plunge phase is lowered. The largest reduction in mean power occurs in the rigid wing. The flexible wing have similar power requirements for −105° and −90° pitch–plunge phases, while power requirements for −75° are slightly higher, presumably due to an increase in lift and drag. The opposite trends in leading edge force are true, where leading edge force is reduced as the phase angle is decreased. As with all other parameter studies considered, the peak leading edge force increases with taper ratio as the wing becomes more flexible. The mean lift-to-power ratio is similar for all phase angles considered, particularly in the range of taper ratios that produce sufficient lift for hovering flight.

5. Discussion

5.1. Optimal lift production

Functionally graded flexural rigidity may improve flight performance in terms of aerodynamic force generation across a broad range of flapping wing kinematics. Figures 7–9 show that the mean lift produced by flexible wings is generally greater than that produced by rigid wings, though rigid wings may outperform flexible wings when deformation is extreme. Interestingly, there is an optimal taper ratio that maximizes the mean lift. For the normal flapping kinematics shown in table 1, this taper ratio is about 0.5, which corresponds to a natural frequency of 83 Hz and a flapping-to-natural frequency ratio of about 0.3. Prior studies show similar aerodynamic benefits when operating close to this ratio. Vanella *et al* showed that flapping at 1/3 the wing's natural frequency evokes a super-harmonic resonant response that improves the lift-to-drag ratio compared to a rigid wing with identical kinematics [2]. Dai *et al* found that flexible wings with flapping-to-natural frequency ratios equal to or less than 0.3 produced more lift than rigid wings [34]. Though our results generally agree with these findings, we saw that the exact lift-maximizing flapping-to-natural frequency ratio depends on flapping kinematics. For a pitching amplitude of 50°, the optimal flapping-to-natural frequency ratio is about 0.27; this increases to about 0.35 when the pitching amplitude is reduced to 40°. The optimal flapping-to-natural ratio changes with pitch–plunge phase as well, but is stationary with respect to plunge amplitude. This collectively shows that the wing's natural frequency is strongly associated with lift generation.

5.2. Trade-offs between power & force

In all cases tested, mean power and peak leading edge force were inversely proportional. With increasing taper ratio, mean power decreased while peak leading edge force increased. The reduction of power at high taper ratios likely stems from a reduction of drag, though lift is lower at higher taper ratios as well. Large leading edge forces at high taper ratios result from the increased deflections and accompanying inertial forces.

The inverse relationship of mean power and peak leading edge force poses trade-offs for flight. Low mean power consumption implies the insect requires less energy storage, and low peak leading edge forces implies that the insect requires less muscle mass. Based on insect anatomy, we hypothesize that the flight mechanism is oriented more towards energetic efficiency. The thorax constitutes about 25%–30% of the total body mass in *M. sexta* [30] and the flight muscles occupy much of the thorax volume. The flight muscles can generate staggering forces, with one flight muscle group producing forces as high as 1 N [35]. These forces are 50 times greater than the total weight of the insect assuming a body mass of 2 grams. It is possible that the increased muscle force requirements resulting from wing flexibility are an acceptable trade-off for high aerodynamic force generation and relatively low power consumption.

5.3. Implications for robotics

The results of this study can inform the design and fabrication of insect-scale flapping wing micro air vehicles (FWMAVs). FWMAVs operating at low Reynolds numbers have reduced payload capacity, which makes conventional sensing and actuation technologies prohibitively heavy or energetically inefficient. Consequently, many FWMAVs rely on external tethers to supply power [16], which limits their autonomy and ability to perform useful tasks. Lightweight, flexible wing structures inspired by flying insects can reduce the power required to flap, thereby improving the energy economy of the robotic vehicle.

Artificial have been fabricated in a variety of ways, including additive manufacturing, laser cutting, molding or a combination thereof [25, 36, 37]. As manufacturing techniques become more sophisticated, the ability to tailor local wing stiffness through geometric or material modifications has improved. The capacity to modulate geometric or material properties may enable artificial wings to behave more similarly to their biological counterparts during flight. Chordwise functional rigidity plays a key role in some insect wings [38], and as shown within this work, may benefit aerodynamic force generation and energetic expenditures. Graded flexural rigidity in artificial wings can be realized by varying the taper ratio of vein structures that serve support scaffolding for surrounding membrane material.

In the design of functionally graded wings, one must first establish the range of taper ratios what produce enough lift to support the aircraft. Trade-offs between peak force and mean power should also be considered. As discussed, mean power and peak force scale inversely with one another as taper ratio is varied. From a robotics perspective, higher mean power draw requires increased energy storage, and larger peak forces require bigger actuators capable of delivering such forces. However, within the permissible range of taper ratios, higher taper ratios correspond to larger mean lift-to-power ratios. We consequently believe that the upper bound of taper ratio that provides enough lift for flight represents a design that balances the various requirements for power and force. However, true three-dimensional simulations should also be performed to understand how physics neglected by this two-dimensional model (e.g., spanwise bending and flow) may also influence wing performance.

5.4. Computational economy and model assumptions

The reduced-order FSI model developed through this work can be used to estimate how morphological or material properties beyond flexural rigidity impact flapping wing performance. Though the pitch–plunge idealization is used frequently to study of flapping wings, most implementations still rely on high-order computational solvers. UVLM has been incorporated into the pitch–plunge model to reduce the computational costs of the fluid solver on several occasions, but the AMM representation is less frequently used to lower the costs of the structural solver. Together, our model based on coupled UVLM/AMM can be solved in less than 1 s per wingbeat for the described discretization parameters, representing a large computational savings compared to higher-order solvers. When running on a laptop with a Ryzen 5800H 3.2 GHz CPU and 16 GB of DDR4 RAM, our model solves in roughly 10 s when considering 20 wing beat cycles. Further, to our knowledge, the flapping wing moments, leading edge forces and power for a flexible wing experiencing pitch–plunge motion have not previously been derived in modal coordinates. If wing deformation is known, these expressions can be used to compute quantities more efficiently than if using the canonical definitions, since spatial and temporal dependence can be decoupled and spatial integrals pre-computed.

While computationally efficient, our FSI model has limitations as well. First, the simplified 2D model neglects some dynamics associated with 3D flapping, such as spanwise bending, spanwise flow and wingtip losses. Previous studies have shown that spanwise flow may positively or negatively influence lift depending on the relative phase between bending and flapping [18]. Spanwise bending may be incorporated in future work and would best be accounted for by modifying plunge to be the sum of rigid body flapping and elastic deformation, where the elastic deformation is a degree-of-freedom to be solved for. Spanwise flow and wingtip losses are more difficult to accommodate in a 2D setting, and consequently 2D models are most appropriate to generate approximate low-fidelity solutions quickly. The validity of the 2D solution, and how spanwise flow and wingtip loss may affect a specific wing configuration, should subsequently be assessed with higher-fidelity 3D modeling. Nonetheless, in many cases results from 2D have agreed with results generated by computational or experimental 3D studies with reasonable accuracy [39–41]. This suggests that at least some of the insights garnered from a 2D study can inform a 3D simulation. Next, the UVLM fluid model neglects viscous effects. While the inviscid assumption is appropriate for a broad range of flying insects including *M. sexta*, fluid viscosity may play a non-trivial role in the flight of very small insects [42]. Finally, the structural model is based on linear assumptions and cannot account for structural nonlinearity. As a result, some dynamic phenomena associated with large deformation may be lost. Further, numerous features observed in real wing structures, such as venation patterns, curvature, corrugation and graded material properties are neglected. Each of these may contribute to the wing's overall flexural rigidity, but should first be studied in isolation before a high-fidelity structural model of the wing is attainable.

6. Conclusion

Flapping insect wings are complex structures that deform from aerodynamic and inertial forces. In addition to the flapping motions of the wing, heterogeneous geometric and material properties influence how the wing deforms. Previous studies have shown that flexural rigidity in some insect wings varies as much as two orders of magnitude from the leading edge to the trailing edge [8]. However, the computational cost of many flapping wing FSI models have precluded us from understanding how these gradients in flexural rigidity regulate flapping wing performance. In this work, we developed a simplified 2D FSI model of a flapping wing as a pitching-plunging airfoil using AMM and UVLM. We derived expressions for the power, leading edge forces and moments required to flap the wing using modal coordinates. We used these models to understand how gradients in flexural rigidity affect flight energetics and the forces needed to sustain flight.

We found that wings with functionally graded flexural rigidity increased aerodynamic force generation and decreased power requirements relative to rigid wings or wings with uniform flexural rigidity. For normal hovering flapping kinematics, a wing with an optimal taper ratio of 0.5 produced about 20% more mean lift than a rigid wing and required about 15% less mean power. This taper ratio corresponded to a wing with a natural frequency of about 85 Hz, which is similar to the torsional natural frequency measured in *M. sexta* wings [25]. Variation of rigid body pitch amplitude and relative pitch–plunge phase affected the taper ratio that maximized lift production. Otherwise, trends in mean lift, mean power and peak leading edge force were not dramatically affected by deviations in flapping kinematics. This work suggests that functionally graded flexural rigidity, driven by spatial variations of wing thickness, enhances the performance of flapping wing insects.

Funding

This research was supported the National Science Foundation under awards Nos. CBET-1855383 and CMMI-1942810 to MJ. Any opinions, findings, and conclusions or recommendations expressed in this material are those of the author(s) and do not necessarily reflect the views of the National Science Foundation.

Data availability statement

The data that support the findings of this study are available upon reasonable request from the authors.

Appendix A. Aerodynamic modeling

This appendix details the derivation of the UVLM approach used to determine the aerodynamic forces acting on the wing. The flow velocity at any point i in space that is induced by a vortex at j is given by the Biot–Savart law:

$$\boldsymbol{V}_{\text{ind}_{i,j}} = \frac{\Gamma_j}{2\pi L^2}\langle (Z_j - Z_i)\boldsymbol{e}_Y + (Y_i - Y_j)\boldsymbol{e}_Z\rangle, \quad \text{(A.1)}$$

where $\boldsymbol{V}_{\text{ind}}$ is the induced velocity, L is the distance between point i and vortex j, Y and Z are the coordinates of i and j in the inertial reference frame, and Γ_j is the circulation of the vortex. Then, according to the Kelvin–Helmholtz theorem for an ideal fluid, the total circulation around a closed contour must remain constant, or

$$\frac{D\Gamma}{Dt} = 0. \quad \text{(A.2)}$$

Flow may not travel through the solid surface of the wing, meaning that the component of velocity normal to the surface is zero. This is represented by

$$(-\dot{\boldsymbol{R}} + \boldsymbol{V}_{\text{ind}}) \cdot \boldsymbol{n} = 0 \quad \text{(A.3)}$$

where $\dot{\boldsymbol{R}}$ is the velocity of the wing's surface in the inertial reference frame and $\boldsymbol{n}$ is the surface normal vector. By simultaneously enforcing the non-penetration condition at all control points on the wing, as well as the Kelvin–Helmholtz condition, the

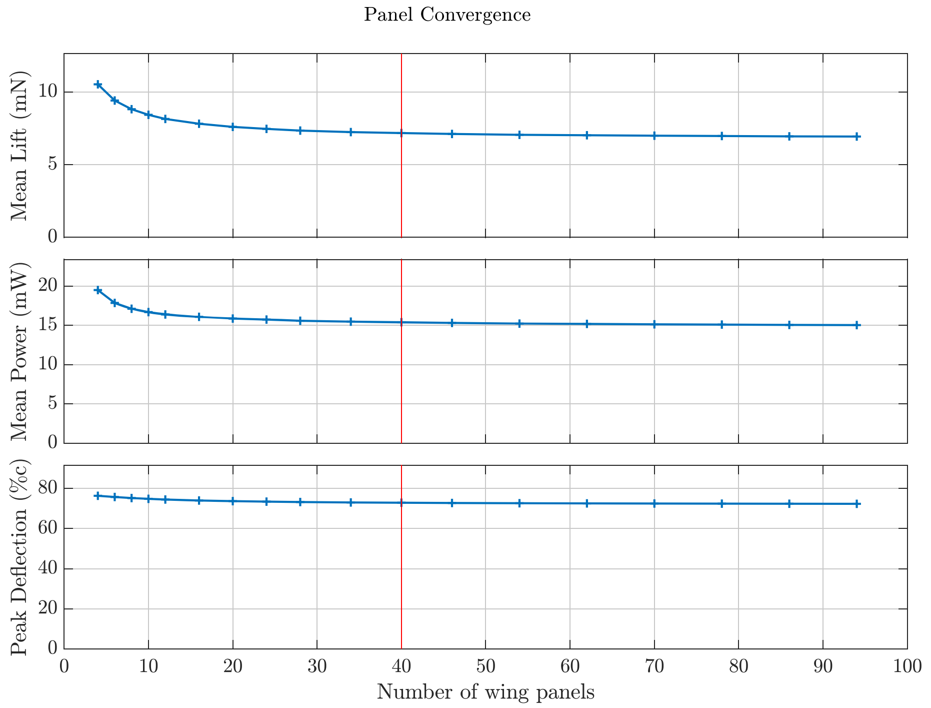

Figure C10. Dependence of mean lift, mean power and peak deflection on chordwise panel discretization. The red line indicates the number of panels used in this work.

strengths of the bound vortices can be determined via

$$\begin{bmatrix} a_{1,1} & a_{1,2} & \dots & a_{1,N_\mathrm{p}} & a_{1,N_\mathrm{p}+1} \\ a_{2,1} & a_{2,2} & \dots & a_{2,N_\mathrm{p}} & a_{2,N_\mathrm{p}+1} \\ \vdots & \vdots & \ddots & \vdots & \vdots \\ a_{N_\mathrm{p},1} & a_{N_\mathrm{p},2} & \dots & a_{Np,N_\mathrm{p}} & a_{Np,N_\mathrm{p}+1} \\ 1 & 1 & \dots & 1 & 1 \end{bmatrix} \begin{Bmatrix} \Gamma_1 \\ \Gamma_2 \\ \vdots \\ \Gamma_{N_\mathrm{p}} \\ \Gamma_{N_\mathrm{p}+1} \end{Bmatrix} = \begin{Bmatrix} \mathrm{rhs}_1 \\ \mathrm{rhs}_2 \\ \vdots \\ \mathrm{rhs}_{N_\mathrm{p}} \\ \mathrm{rhs}^* \end{Bmatrix} \tag{A.4}$$

where $a_{i,j}$ is the influence coefficient. On the right-hand side, $\mathrm{rhs}_{1,2\ldots N_\mathrm{p}}$, are the normal velocities due to the combined effect of the pitch–plunge motion, structural deflection, and velocity induced by the wake vortices. rhs^* is the total bound vorticity from the previous time step. The solved quantities $\Gamma_{1,2\ldots N_\mathrm{p}}$ and $\Gamma_{N_\mathrm{p}+1}$ are the strengths of the bound vortices on the wing and of the newly-shed wake vortex, respectively.

The new wake vortex is placed a fixed distance aft of the trailing edge. All existing wake vortices are advected with the local flow. The velocity of the ith wake vortex is given by

$$\boldsymbol{V}_i = \sum_{j=1}^{N_\mathrm{p}} \boldsymbol{V}_{\mathrm{ind}_{i,j}} + \sum_{k=1,k\neq i}^{N_w} \boldsymbol{V}_{\mathrm{ind}_{i,k}}, \tag{A.5}$$

where $\boldsymbol{V}_i$ is the total induced velocity at i by N_p bound vortices on the wing and $N_\mathrm{w}-1$ wake vortices. A wake vortex is not influenced by its own vorticity. The aerodynamic force on the wing is determined using the unsteady Bernoulli equation,

$$\frac{P_\mathrm{ref}-P}{\rho} = \frac{V^2-V_\mathrm{ref}^2}{2} + \frac{\partial\Phi}{\partial t}, \tag{A.6}$$

where P and P_ref are the local and reference pressures, V and V_ref are the local and reference (freestream) velocities, ρ is the fluid density, and Φ is the flow potential. When solved at the bound vortex for the ith wing panel, this becomes

$$\Delta P_i = -\rho\left[(-\dot{\boldsymbol{R}} + \boldsymbol{V}_{\mathrm{ind,\,i}})\cdot\boldsymbol{\tau}_i\frac{\Gamma_i}{\mathrm{d}s} + \frac{\partial}{\partial t}\sum_{j=1}^{i}\Gamma_j\right] \tag{A.7}$$

where ΔP is the pressure difference between the top and bottom surfaces of the wing and $\boldsymbol{\tau}$ is the unit vector tangent to the wing surface. The total aerodynamic force is obtained by summing the products of the pressure differentials and the panel normal vectors.

Appendix B. Finite element modeling

This appendix details how the mode shapes and natural frequencies of the 2D wing are determined. The stiffness matrix $\mathbf{K}_\mathrm{e}$ based on Euler–Bernoulli beam theory for an individual element is

$$\mathbf{K}_\mathrm{e} = \frac{E_eI_\mathrm{e}}{c_\mathrm{e}^3}\begin{bmatrix} 12 & 6c_\mathrm{e} & -12 & 6c_\mathrm{e} \\ 6c_\mathrm{e} & 4c_\mathrm{e}^2 & -6c_\mathrm{e} & 2c_\mathrm{e}^2 \\ -12 & -6c_\mathrm{e} & 12 & -6c_\mathrm{e} \\ 6c_\mathrm{e} & 2c_\mathrm{e}^2 & -6c_\mathrm{e} & 4c_\mathrm{e}^2 \end{bmatrix} \tag{B.1}$$

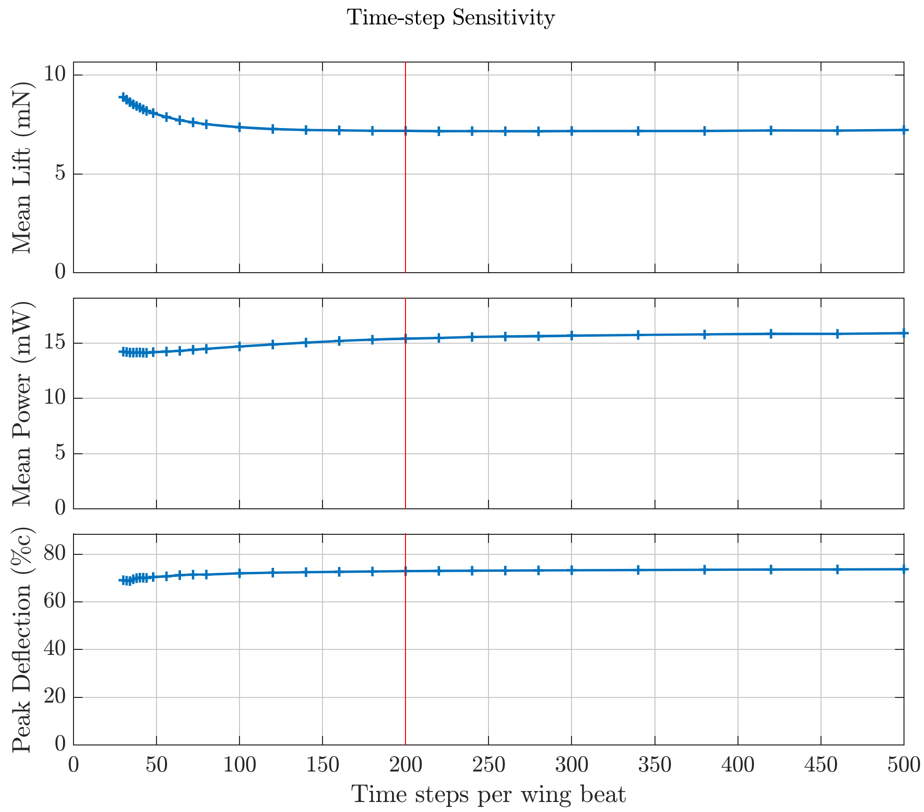

Figure C11. Dependence of mean lift, mean power and peak deflection on time step discretization. The red line indicates the number of panels used in this work.

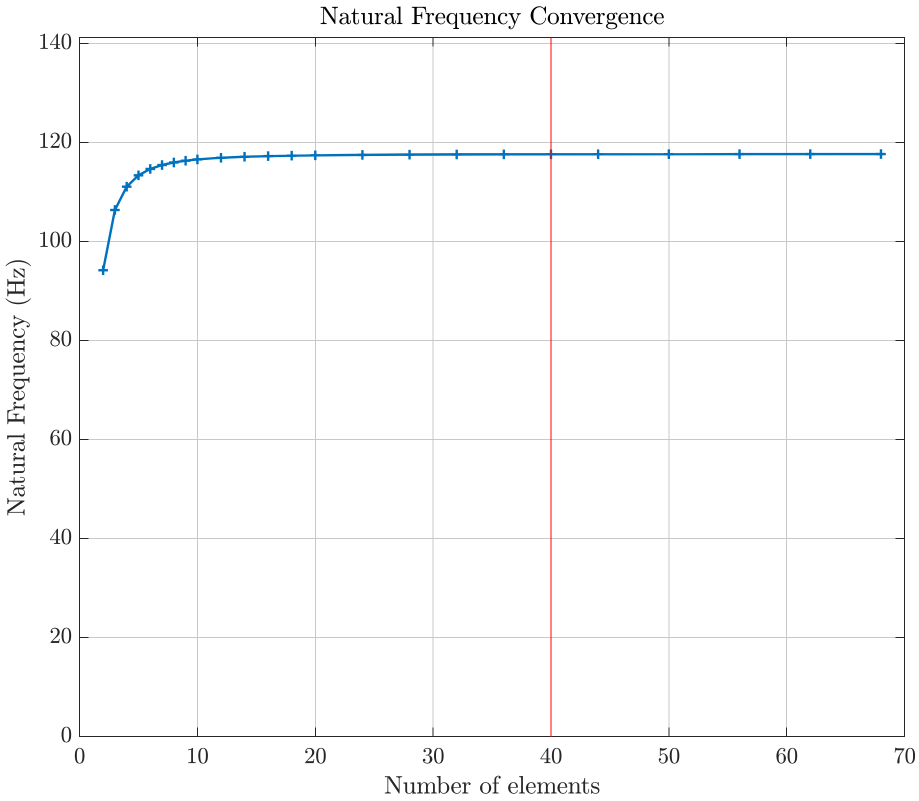

Figure C12. Dependence of the wing's first natural frequency on the number of elements. The red line indicates the number of elements used in this work.

Table C3. Discretization parameters.

Symbol	Description	Value
N_e	Number of elements	40
N_p	Number of panels	40
N_w	Number of wake vortices	100
$T/\mathrm{d}t$	Time-steps per cycle	200

where I_e, E_e, and c_e are the elemental area moment of inertia, elastic modulus, and length respectively. In the I_e calculation, the cross-sectional area of the wing in the x–z plane is assumed rectangular. E_e and c_e are uniform across all elements. The elemental mass matrix $\mathbf{M}_\mathrm{e}$ is

$$\mathbf{M}_\mathrm{e} = \frac{\rho_w b t_e c_e}{420}\begin{bmatrix} 156 & 22c_\mathrm{e} & 54 & -13c_\mathrm{e} \\ 22c_\mathrm{e} & 4c_\mathrm{e}^2 & 13c_\mathrm{e} & -3c_\mathrm{e}^2 \\ 54 & 13c_\mathrm{e} & 156 & -22c_\mathrm{e} \\ -13c_\mathrm{e} & -3c_\mathrm{e}^2 & -22c_\mathrm{e} & 4c_\mathrm{e}^2 \end{bmatrix} \tag{B.2}$$

where ρ_w is the wing material density, b is the wing span, and t_e is the element thickness. The wing vibration modes and natural frequencies are determined by finding the eigenvectors and eigenvalues of the matrix quantity $\mathbf{M}^{-1}K$.

Appendix C. Discretization parameter convergence studies

This appendix shows the convergence studies used to determine panel count, number of time steps and number of elements. All discretization parameters are shown in table C3. Sensitivity of lift, power, and deflection as a function panel count are shown in figure C10, and as a function of time step size in figure C11. The wing's first natural frequency as a function of element count is shown in figure C12. In both the panel count and time step analyses, a homogeneous wing is used, as the most flexible wing should experience the greatest deformation and dependence on panel count. In the element count analysis, a highly-tapered wing is used, since natural frequency converges fastest with the homogeneous wing. In the time-step sensitivity analysis, the number of time-steps per wing beat is varied from 30 to 500. The number of wake vortices N_w was fixed to half of this value to prevent the results being affected by the wing flying back through its wake.

Appendix D. Validation

In this section, we benchmark our model using results from high fidelity CFD from [7]. The two-dimensional wing is uniform thickness and stiffness. The pitch and plunge amplitudes are 22.5° and 1.25c, respectively. The driving-to-natural frequency ratio is 0.4, and the mass number (a measure of the relative magnitude of inertial to aerodynamic forces) is 1. We use the same geometric parameters as shown in table 1, as the comparison study used non-dimensional quantities. We apply low-pass filter to the lift coefficient with a cutoff frequency about 16 times that of the flapping frequency.

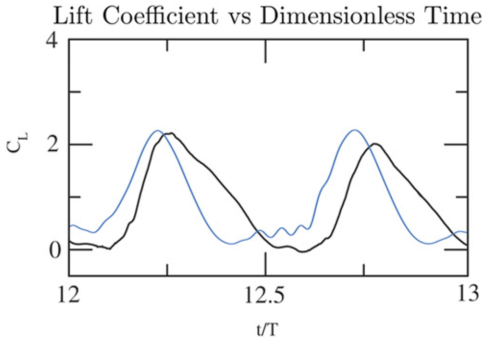

Figure D13. Lift coefficient over a single wing beat from UVLM (blue) and CFD [7] (black).

We compare then the lift coefficient predicted by both models using the maximum plunge rate as the reference velocity (figure D13). Both methods results in similar lift coefficients, though the lift coefficient by UVLM slightly lags the phase of that predicted by the higher fidelity model. Given the computational savings of the reduced-order model, we consider these results to be sufficiently similar.

ORCID iDs

Mark Jankauski https://orcid.org/0000-0001-6305-0564

References

[1] Combes S A and Daniel T L 2003 Into thin air: contributions of aerodynamic and inertial-elastic forces to wing bending in the Hawkmoth Manduca sexta *J. Exp. Biol.* **206** 2999–3006

[2] Vanella M, Fitzgerald T, Preidikman S, Balaras E and Balachandran B 2009 Influence of flexibility on the aerodynamic performance of a hovering wing *J. Exp. Biol.* **212** 95–105

[3] Mountcastle A and Daniel T 2010 Vortexlet models of flapping flexible wings show tuning for force production and control *Bioinspir. Biomim.* **5** 045005

[4] Mountcastle A M and Combes S A 2013 Wing flexibility enhances load-lifting capacity in bumblebees *Proc. R. Soc.* B **280** 20130531

[5] Jankauski M, Guo Z and Shen I 2018 The effect of structural deformation on flapping wing energetics *J. Sound Vib.* **429** 176–92

[6] Reid H E, Schwab R K, Maxcer M, Peterson R K, Johnson E L and Jankauski M 2019 Wing flexibility reduces the energetic requirements of insect flight *Bioinspir. Biomim.* **14** 056007

[7] Yin B and Luo H 2010 Effect of wing inertia on hovering performance of flexible flapping wings *Phys. Fluids* **22** 111902

[8] Combes S and Daniel T 2003 Flexural stiffness in insect wings II. Spatial distribution and dynamic wing bending *J. Exp. Biol.* **206** 2989–97

[9] Tian F-B, Dai H, Luo H, Doyle J F and Rousseau B 2014 Fluid–structure interaction involving large deformations: 3D simulations and applications to biological systems *J. Comput. Phys.* **258** 451–69

[10] Ishihara D, Horie T and Denda M 2009 A two-dimensional computational study on the fluid–structure interaction cause of wing pitch changes in dipteran flapping flight *J. Exp. Biol.* **212** 1–10

[11] Hamamoto M, Ohta Y, Hara K and Hisada T 2007 Application of fluid–structure interaction analysis to flapping flight of insects with deformable wings *Adv. Robot.* **21** 1–21

[12] Fitzgerald T, Valdez M, Vanella M, Balaras E and Balachandran B 2011 Flexible flapping systems: computational investigations into fluid–structure interactions *Aeronaut. J.* **115** 593–604

[13] Tang J, Chimakurthi S, Palacios R, Cesnik C and Shyy W 2008 Computational fluid–structure interaction of a deformable flapping wing for micro air vehicle applications *46th AIAA Aerospace Sciences Meeting and Exhibit* vol 615

[14] Jankauski M and Shen I 2014 Dynamic modeling of an insect wing subject to three-dimensional rotation *Int. J. Micro Air Vehicles* **6** 231–51

[15] Anderson J D and Wendt J 1995 *Computational Fluid Dynamics* vol 206 (Berlin: Springer)

[16] Platzer M F, Jones K D, Young J and Lai J C 2008 Flapping wing aerodynamics: progress and challenges *AIAA J.* **46** 2136–49

[17] Tian F-B, Luo H, Song J and Lu X-Y 2013 Force production and asymmetric deformation of a flexible flapping wing in forward flight *J. Fluids Struct.* **36** 149–61

[18] Roccia B A, Preidikman S, Verstraete M L and Mook D T 2017 Influence of spanwise twisting and bending on lift generation in MAV-like flapping wings *J. Aerospace Eng.* **30** 04016079

[19] Birch J M and Dickinson M H 2001 Spanwise flow and the attachment of the leading-edge vortex on insect wings *Nature* **412** 729–33

[20] Kweon J and Choi H 2010 Sectional lift coefficient of a flapping wing in hovering motion *Phys. Fluids* **22** 071703

[21] Hoffmann J, Donoughe S, Li K, Salcedo M K and Rycroft C H 2018 A simple developmental model recapitulates complex insect wing venation patterns *Proc. Natl Acad. Sci. USA* **115** 9905–10

[22] Reade J and Jankauski M A 2020 Deformable blade element and unsteady vortex lattice fluid–structure interaction modeling of a 2D flapping wing *Int. Design Engineering Technical Conf. Computers and Information in Engineering Conf.* vol 83969 (American Society of Mechanical Engineers) V007T07A032

[23] Katz J and Plotkin A 2001 *Low-Speed Aerodynamics* vol 13 (Cambridge: Cambridge University Press)

[24] Willmott A P and Ellington C P 1997 The mechanics of flight in the Hawkmoth Manduca sexta. I. Kinematics of hovering and forward flight *J. Exp. Biol.* **200** 2705–22

[25] Reid H, Zhou H, Maxcer M, Peterson R K, Deng J and Jankauski M 2021 Toward the design of dynamically similar artificial insect wings *Int. J. Micro Air Vehicles* **13**

[26] Casey C, Yager C, Jankauski M and Heveran C M 2022 The flying insect thoracic cuticle is heterogeneous in structure and in thickness-dependent modulus gradation *Acta Biomaterialia* 422–9

[27] Vincent J and Wegst U 2004 Design and mechanical properties of insect cuticle *Arthropod Struct. Dev.* **33** 187–99

[28] Norris A G, Palazotto A N and Cobb R G 2013 Experimental structural dynamic characterization of the hawkmoth (Manduca sexta) forewing *Int. J. Micro Air Vehicles* **5** 39–54

[29] Bergou A J, Xu S and Wang Z J 2007 Passive wing pitch reversal in insect flight *J. Fluid Mech.* **591** 321–37

[30] Hedrick T L and Daniel T 2006 Flight control in the Hawkmoth Manduca sexta: the inverse problem of hovering *J. Exp. Biol.* **209** 3114–30

[31] Altshuler D L, Dickson W B, Vance J T, Roberts S P and Dickinson M H 2005 Short-amplitude high-frequency wing strokes determine the aerodynamics of honeybee flight *Proc. Natl Acad. Sci. USA* **102** 18213–8

[32] Schmitz S 2020 *Aerodynamics of Wind Turbines: A Physical Basis for Analysis and Design* (New York: Wiley)

[33] Ando N and Kanzaki R 2016 Flexibility and control of thorax deformation during Hawkmoth flight *Biol. Lett.* **12** 20150733

[34] Dai H, Luo H and Doyle J F 2012 Dynamic pitching of an elastic rectangular wing in hovering motion *J. Fluid Mech.* **693** 473–99

[35] Tu M S and Daniel T L 2004 Submaximal power output from the dorsolongitudinal flight muscles of the Hawkmoth Manduca sexta *J. Exp. Biol.* **207** 4651–62

[36] Tanaka H and Wood R J 2010 Fabrication of corrugated artificial insect wings using laser micromachined molds *J. Micromech. Microeng.* **20** 075008

[37] Pornsin-Sirirak T N, Tai Y, Nassef H and Ho C 2001 Titanium-alloy MEMS wing technology for a micro aerial vehicle application *Sensors Actuators* A **89** 95–103

[38] Combes S and Daniel T 2003 Flexural stiffness in insect wings I. Scaling and the influence of wing venation *J. Exp. Biol.* **206** 2979–87

[39] Wang Z J, Birch J M and Dickinson M H 2004 Unsteady forces and flows in low Reynolds number hovering flight: two-dimensional computations vs robotic wing experiments *J. Exp. Biol.* **207** 449–60

[40] Whitney J P and Wood R J 2010 Aeromechanics of passive rotation in flapping flight *J. Fluid Mech.* **660** 197–220

[41] Liu L and Sun M 2018 The added mass forces in insect flapping wings *J. Theor. Biol.* **437** 45–50

[42] Santhanakrishnan A, Robinson A K, Jones S, Low A A , Gadi S, Hedrick T L and Miller L A 2014 Clap and fling mechanism with interacting porous wings in tiny insect flight *J. Exp. Biol.* **217** 3898–909